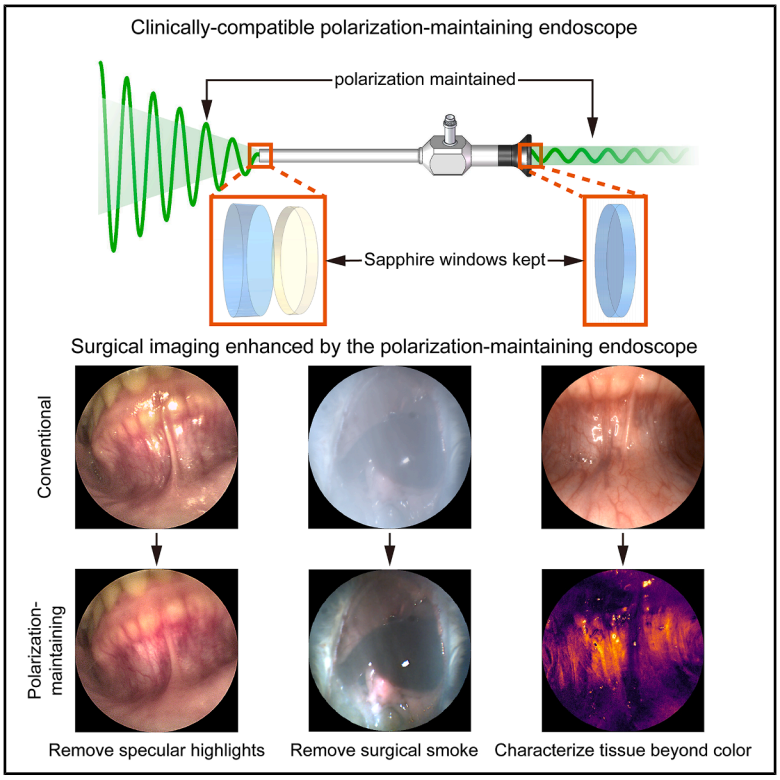
Device

Article

A polarization-maintaining endoscope for surgical imaging

Graphical abstract



Highlights

- Study on the polarization effects of conventional endoscopes and their origin
- Aperture depolarization to explain bandwidth-insensitive depolarization
- Method for constructing polarization-maintaining endoscope suitable for clinical use
- Specularity/smoke removal and polarimetry error cut by polarization-maintaining endoscope

Authors

Jiawei Song (宋嘉伟), Daqian Wang (王大千), Changjiang Zhou (周长江), ..., Xiaocong Yuan (袁小聪), Qing Yang (杨青), Ji Qi (祁绩)

Correspondence

xcyuan@zhejianglab.org (X.Y.), qingyang@zju.edu.cn (Q.Y.), ji.qi@zhejianglab.org (J.Q.)

In brief

Song et al. present a technique to achieve a polarization-maintaining endoscope that is compatible with the sapphire windows used in standard clinical endoscope design by developing a birefringence compensation approach. Using this device, the polarization-resolved imaging methods can be implemented in endoscopy *in vivo*. Polarization-resolved endoscopy with this device enhances surgical imaging by removing specularities, improving the image visibility affected by surgical smoke, and enabling accurate polarimetric endoscopy for tissue characterization, supporting precise detection and intelligent operation during minimally invasive surgery.

4 Validate
Functional device with real-world testing, ready to scale

Song et al., 2025, Device *3*, 100871
November 21, 2025 © 2025 The Author(s).
Published by Elsevier Inc.
https://doi.org/10.1016/j.device.2025.100871

CellPress

Device

CellPress
OPEN ACCESS

Article

A polarization-maintaining endoscope for surgical imaging

Jiawei Song (宋嘉伟),[1] Daqian Wang (王大千),[1] Changjiang Zhou (周长江),[1] Yongtai Chen (陈永台),[1] Fei Guo (郭飞),[1] Liqiang Wang (王立强),[2] Daniel S. Elson,[3] Xiaocong Yuan (袁小聪),[1,*] Qing Yang (杨青),[2,*] and Ji Qi (祁绩)[1,4,*]

[1]Research Center for Frontier Fundamental Studies, Zhejiang Lab, Hangzhou, China

[2]State Key Laboratory of Extreme Photonics and Instrumentations, College of Optical Science and Engineering, Zhejiang University, Hangzhou, China

[3]Hamlyn Center for Robotic Surgery & Department of Surgery and Cancer, Imperial College London, London, UK

[4]Lead contact

*Correspondence: xcyuan@zhejianglab.org (X.Y.), qingyang@zju.edu.cn (Q.Y.), ji.qi@zhejianglab.org (J.Q.)

https://doi.org/10.1016/j.device.2025.100871

THE BIGGER PICTURE Endoscopic imaging is crucial during minimally invasive surgeries. However, conventional endoscopy may produce poor-quality images due to the glare from moist tissues and smoke from surgical ablation. It also suffers from difficulty detecting abnormal tissue that lacks color contrast. These issues make it difficult for surgeons to see clearly as well as increase risks for patients. Polarization imaging offers a promising solution to address these issues, but standard endoscopes introduce optical effects that interfere with polarization imaging. Here, we develop a polarization-maintaining endoscope that is compatible with polarization imaging methods. We demonstrate that polarization imaging based on this endoscope can remove glare in real time, improve image clarity by 73% in smoky conditions, and achieve a 3-fold increase in accuracy for tissue-polarization measurements, thus enhancing the ability to detect lesions with low color contrast.

SUMMARY

Standard-of-care endoscopy is prone to image-quality degradation from specular reflections and surgical smoke as well as misdetection of lesions lacking color features, which diminish precision and pose risks for surgery. Integrating polarization-resolved imaging with endoscopy holds great promise to address these challenges, but conventional endoscopes have complex polarization properties that interfere with polarization-resolved imaging. Here, we demonstrate a polarization-maintaining endoscope (PME) that maintains the polarization state of the incident light under broadband illumination. The PME resolves the conflict between maintaining polarization and incorporating sapphire windows—an important element for ensuring clinical compatibility but polarization disruption. We show that using the PME can enhance surgical imaging *in vivo* by eliminating specular highlights in real time, enhancing the visibility of images affected by surgical smoke by a factor of 1.7, and improving the accuracy of polarimetric endoscopy 3-fold, aiding in the characterization of tissues beyond color for tumor detection.

INTRODUCTION

Surgical endoscopes are essential instruments that provide visual information within body cavities such as the abdomen and enable surgeons to observe the surgical field, identify anatomical structures, and locate lesions during minimally invasive surgeries. Conventional endoscopy, known as white-light endoscopy (WLE), utilizes white-light illumination and color imaging that closely mimics human vision. As a color-resolved technique, it provides intuitive and informative visuals. However, the quality of WLE images is often degraded by the complex surgical environments, such as specular reflection, known as "specularities," and surgical smoke. The specularities arising from smooth and moist tissue surfaces may obstruct important information and introduce confusing features that may be falsely interpreted. The smoke caused by electrified surgical instruments deteriorates visibility and obscures targets. Quality degradation of the WLE images poses risks in minimally invasive surgery (MIS)[1–3] and limits the capability of computer vision and AI algorithms that are important for the support of surgery approaches

This is an open access article under the CC BY-NC license (http://creativecommons.org/licenses/by-nc/4.0/).

including augmented-reality and robotic surgeries.[4–6] The WLE method is often insufficiently accurate for detecting early-stage cancer tumors and lesion margins, due to the lack of discernible color contrast or texture features.[7,8]

To overcome challenges caused by image degradation, efforts have been concentrated on computational approaches for image restoration. These approaches leverage correlations in different domains: spatial, which are within the neighborhood of specularities; temporal, which utilize neighboring frames where specularities appear at different locations; or color space, where the dark channels are used for smoke-thickness estimation.[4,6–9] However, learning-based restoration approaches encounter challenges including a lack of training data, absence of ground truth, and lack of interpretability, while the model-based methods rely on manually tuned parameters, which are susceptible to local minima and result in low output quality. To enhance tissue characterization and lesion detection, several techniques have been developed by leveraging the properties of light beyond color, including optical coherence tomography,[10,11] endoscopic light-scattering spectroscopy,[12,13] laser scanning confocal endomicroscopy,[14,15] and non-linear microscopy.[16] These methods require a long scanning time, which poses challenges for intraoperative imaging of dynamic and deforming surgical scenes.

Integrating polarization-resolved imaging techniques with the standard-of-care WLE holds great potential for addressing the aforementioned long-standing challenges, considering that polarization can be utilized to differentiate reflected light from multiple scattered light (based on the polarization gated imaging technique), enhance obscured targets within turbid media (based on computational polarization imaging techniques), and examine anisotropic structures such as collagen that serve as key imaging biomarkers for tumor detection (based on the polarimetric imaging technique).[17–22] However, the complex polarization effects of conventional endoscopes disrupt polarization-resolved imaging modalities. These polarization properties, associated with the birefringent sapphire windows in the endoscopes, are not yet well understood and are not easily compensated by calibration in polarimetry. Substituting sapphire with non-birefringent materials has been carried out to obtain proof-of-concept endoscopes suitable for polarization-resolved imaging.[21,23] Nonetheless, sapphire is important to ensure reliable tightness, required by clinical devices involving the harsh conditions of sterilization and chemical erosion,[24] because it is weldable and thereby suitable for permanent sealing.[25] A viable solution to achieve a clinically compatible polarization-maintaining endoscope (PME) with minimal interference to polarization-resolved imaging has not yet been developed.[21,23,26–31]

In this study, we explored the origin of the polarization effects in conventional endoscopes. Based on a better understanding of the mechanisms, we demonstrate a broadband prototype PME that resolves the conflict between maintaining polarization and incorporating sapphire windows. With the PME, polarization-resolved imaging can then be conducted in real time with high definition. It is shown that using the PME can enhance surgical imaging *in vivo* by removing specularities, improving the image visibility affected by surgical smoke, and enabling accurate polarimetric endoscopy for tissue characterization, supporting precise detection and intelligent operation during MIS.

Background

Conventional surgical endoscopes exhibit significant retardance and depolarization effects, which interfere with polarization-resolved imaging techniques, leading to image artifacts and polarimetric errors (for details about the interference to polarization-resolved imaging, refer to Note S1). As a result, polarization-resolved imaging cannot be effectively implemented using conventional endoscopes. Through experimental analysis (see Note S2), it can be concluded that the retardance and depolarization originate from the sapphire windows of the endoscopes. Key factors deciding the magnitude and spatial distribution of these effects include the thickness of the sapphire window, the orientation of its optical axis (OA), its position within the optical system, and the angular field of view (AFOV) of the endoscope.

A model that explains the origin of the retardance of conventional endoscopes are provided in Notes S3 and S4, and a comparison of the results from experiments and simulation are presented in Figure 1. The retardance patterns with C-, A-, and R-cut windows (referring to OA directions perpendicular, parallel to window surface, and in between) were simulated and are shown in Figure 1B, and they agree with those obtained experimentally (Figures S1A–S1C). Other factors including the thickness, AFOV, and wavelength were examined (Figures 1C–1E), and the patterns obtained from simulations were consistent with the experiment (Figures S1H–S1M). The retardance order and phase are dependent on wavelength (Figure 1G). Therefore, the incoherent superposition of light affected by wavelength-dependent retardance over the spectrum would result in depolarization (Figures 1F and 1H). In this study, this was termed chromatic depolarization. Previously, bandwidth-dependent depolarization has been observed but not fully understood.[26] The model provided here explains the formation mechanism and the featured distribution of chromatic depolarization. Based on the model, the chromatic depolarization for both C- and A-cut windows under broadband illumination (full width at half maximum [FWHM] = 200 nm) were simulated. The simulation (see Note S5) generated radially increasing depolarization for the C-cut window and homogeneous depolarization for the A-cut window, in agreement with the experiments (Figure 1I).

Besides the chromatic depolarization, there is also bandwidth-insensitive depolarization in the field of view (FOV). Here, we propose a complementary depolarization formation mechanism termed aperture depolarization. As shown in Figure 1J, the aperture depolarization is defined by the entrance pupil of the endoscope. The entrance pupil allows a cone of rays from a specific object point that transmit through the endoscope. Each individual ray within the cone propagated along a different angle with respect to the OA direction and underwent slightly different retardance. Subsequently, when these rays converged into an image point, their incoherent superposition led to bandwidth-insensitive depolarization. Based on the model, the aperture depolarization with both C- and A-cut sapphire windows was simulated (see Note S6), and the results agreed with the experiments. As shown by the results (Figure 1M), the C-cut window featured a radially increasing aperture depolarization with

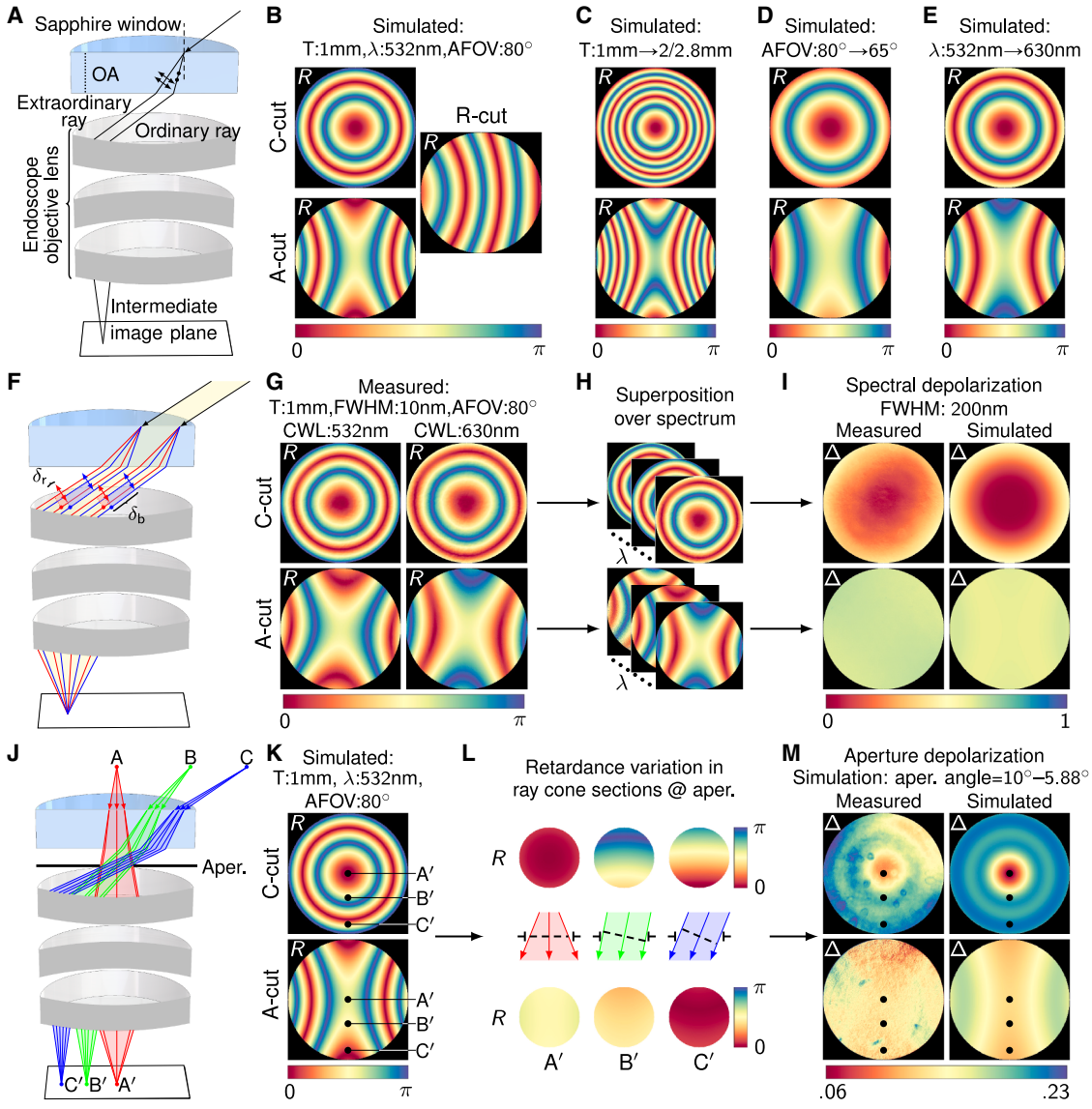


Figure 1. Underlying mechanism causing polarization effects in conventional endoscopes

(A) Formation of retardance due to sapphire-window birefringence.

(B–E) Simulated retardance patterns based on our model with the following conditions: (B) $T = 1$ mm, $\lambda = 532$ nm, AFOV = 80°, and different OA directions; (C) $T = 2$ mm for C-cut and 2.8 mm for A-cut windows, $\lambda = 532$ nm, AFOV = 80°; (D) $T = 1$ mm, $\lambda = 532$ nm, AFOV = 65° for C- and A-cut windows; (E) $T = 1$ mm, $\lambda = 630$ nm, AFOV = 80° for C- and A-cut windows.

(F) Formation of the chromatic depolarization.

(G) Retardance patterns of the experimental endoscope with 1-mm C- and A-cut sapphire windows and 80° AFOV depending on the wavelength of the light source (center wavelength [CWL] = 532 nm and 630 nm; FWHM = 10 nm).

(H) Incoherent superposition of light affected by the wavelength-dependent retardance over the spectrum.

(I) Comparison between the measured and simulated chromatic depolarization.

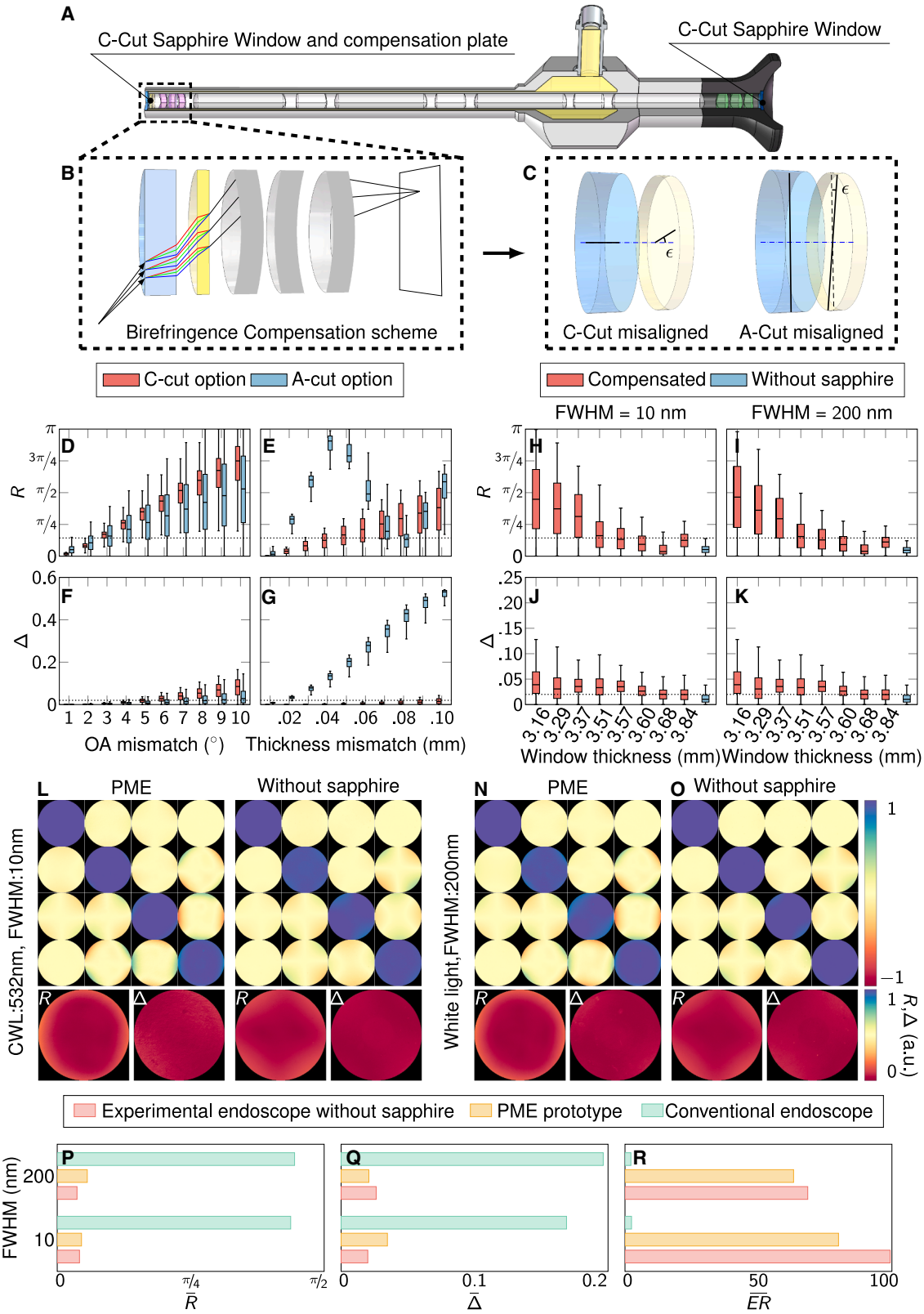
(J) Formation of aperture depolarization.

(K) Simulated retardance for C- and A-cut windows based on our model with $T = 1$ mm, $\lambda = 532$ nm, AFOV = 80°.

(L) Retardance variation in the cross-section of the ray cone.

(M) Comparison of the measured and simulated aperture depolarization.

concentric rings indicating relatively lower depolarization, while A-cut windows featured a relatively lower depolarization strip perpendicular to the OA direction. The depolarizations of three representative points along the radius (Figure 1K) were examined. For the C-cut windows, since the retardance variation frequency in the cross-section of the ray cone increased radially (Figure 1L), the aperture depolarization was stronger in the peripheral region (compare C′ and A′ in Figure 1L). However, in



(legend on next page)

regions where the frequency was moderate, the aperture depolarization became weaker and signature rings appeared. For the A-cut window, the aperture depolarization marked a weak depolarization stripe owing to the low fringe frequency, and the depolarization was weaker at the peripheral region (C′) than at the center (A′) because the aperture angle was smaller in the peripheral region. The aperture depolarization accounted for approximately 37% of the total depolarization despite being generally weaker than chromatic depolarization (Figures S5J and S5K).

RESULTS AND DISCUSSION

Maintaining polarization using birefringence compensation

According to investigation of the polarization effects of the conventional endoscope, it is clear that the birefringence of the sapphire windows causes inhomogeneous retardance in both spatial and spectral domains and that this inhomogeneous retardance further results in chromatic and aperture depolarization. Therefore, by suppressing the retardance, the undesirable polarization effects of the conventional endoscope can be mitigated. Owing to the requirements for clinical use, the solution should address the issue with the sapphire windows retained in the endoscope.

To suppress the polarization effects at the proximal end, we proposed using a C-cut sapphire plate as the proximal window, as it induced negligible polarization effects (Figure S2F). To mitigate the polarization effects at the distal end, we inserted a compensating plate made from a crystal with the opposite birefringence to sapphire between the sapphire window and the objective (Figures 2A and 2B). Given that sapphire has negative birefringence, magnesium fluoride (MgF_2), with positive birefringence, was selected for the compensation, since their birefringence spectra are highly complementary (Figure S6). Moreover, the compensation plate should be in the OA direction parallel to the sapphire window. Two compensation options were possible, the A-cut (A-cut sapphire and MgF_2) and C-cut (C-cut sapphire and MgF_2), with optimal thickness ratios between the sapphire and MgF_2 plates determined via simulation to be 2.29 and 2.43, respectively.

Considering that OA and thickness mismatches between the sapphire and MgF_2 plates are inevitable during production (Figure 2C), tolerance to the mismatches is calculated (see Note S7) as presented in Figures 2D–2G, and the threshold for the remaining retardance and depolarization were set to 0.26 rad and 0.02, respectively, which are determined based on the experimental endoscope without sapphire windows (i.e., non-depolarizing). The tolerances to the OA mismatch were 2° and 1.5° for C- and A-cut windows, respectively, regarding the retardance (Figure 2D), and about 5.2° and 8.8° for C- and A-cut windows, respectively, regarding the depolarization (Figure 2F). For the thickness mismatch, the tolerance was about 0.03 mm and 0.02 mm for C- and A-cut windows, respectively for retardance (Figure 2E) and was about 0.10 mm and 0.02 mm for the C- and A-cut windows, respectively, for depolarization (Figure 2G). All the tolerances here well exceed the typical precision of optical manufacturing and assembly, but the C-cut compensation is generally more tolerant to mismatches and is thus preferred.

To validate the proposed solution, a prototype PME was constructed with C-cut sapphire windows and MgF_2 compensation plate. A 1.60-mm MgF_2 plate was paired with sapphire windows whose thickness ranged from 3.16 to 3.84 mm at the distal end of the experimental endoscope, and the resulting polarization effects of the endoscope (Figures 2H–2K) were measured with the benchtop Mueller imaging system (see Notes S8 and S9). Among the sapphire windows, the 3.68-mm window was the optimal match to the MgF_2 plate, and they had a thickness ratio of 2.30, close to the theoretical optimum of 2.29. To build the PME prototype, we employed this pair at the distal end of the endoscope and a 1-mm C-cut sapphire window at the proximal end, and the AFOV was limited to 70°.

The polarization effects of the PME prototype were measured with light sources of different spectral bandwidths and were compared to those of the experimental endoscope without sapphire windows and a representative conventional endoscope (ShenDa, Figures 2L–2O and S5). The Mueller matrices of the PME were close to the identity matrices under both narrow and broad bandwidths, indicating its superior performance in maintaining polarization. The decomposed results quantitatively revealed that the PME had average retardance below 0.18 rad and average depolarization below 0.03 in the FOV, reaching a level similar to that in the experimental endoscope (Figures 2P–2R). Contrarily, the average depolarization and retardance of the conventional endoscope were nearly ten times higher than those in the PME. To assess the quality of

Figure 2. Proposed birefringence compensation method for constructing the polarization-maintaining endoscope and its subsequent polarization effects

(A) Optical structure of a polarization-maintaining endoscope (PME) with sapphire windows in place.

(B) Distal end optics of the PME.

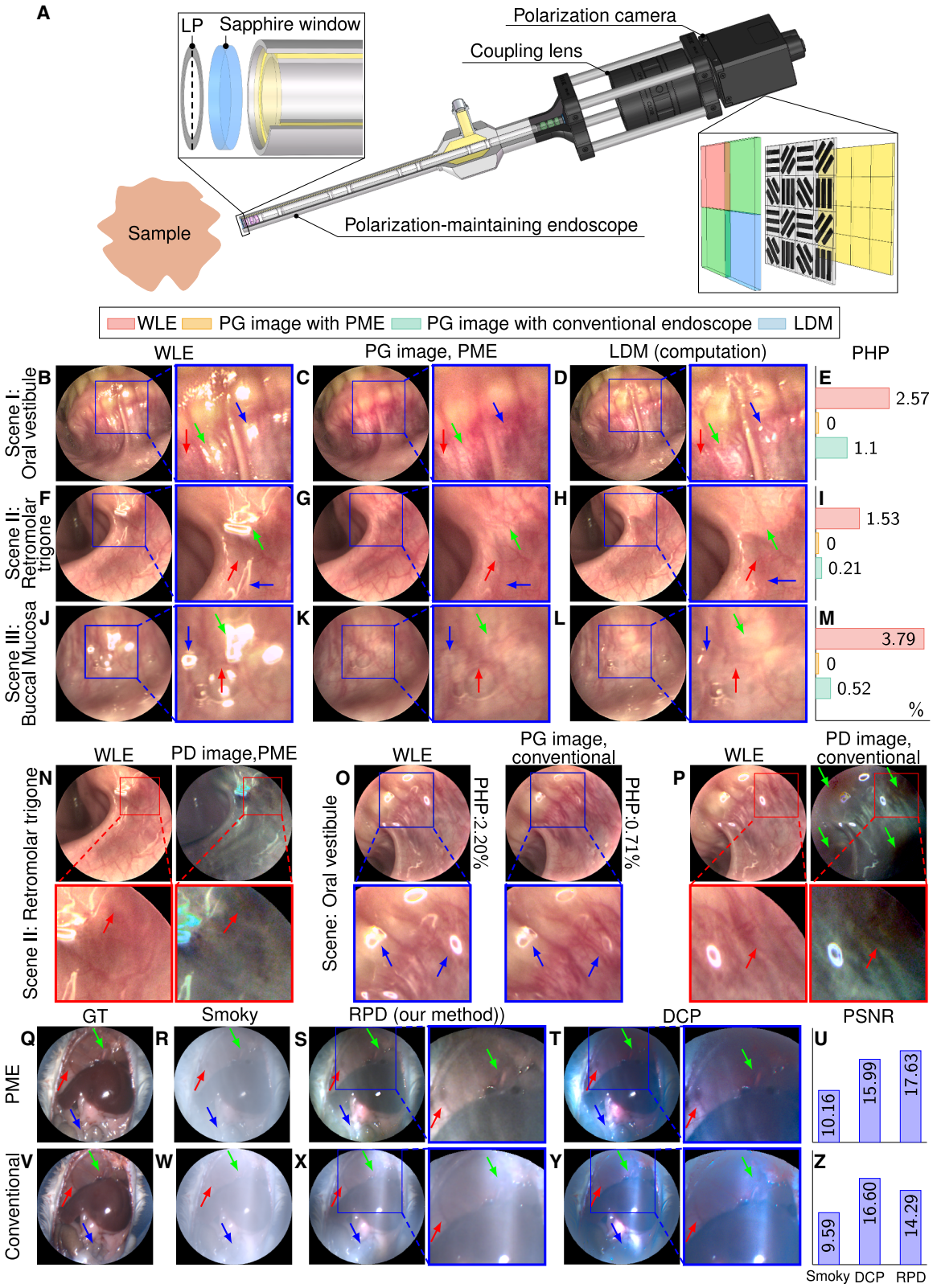
(C) Possible OA mismatches in the compensation.

(D–G) (D and E) Simulated retardance of the endoscope with OA (D) and thickness (E) mismatch between the sapphire window and the compensation plate. (F and G) Simulated depolarization of the endoscope with OA (F) and thickness (G) mismatch. The dotted lines indicate the tolerance for the remaining retardance and depolarization of the endoscope after compensation.

(H–K) Residual retardance (H and I) and depolarization (J and K) in the endoscope when the 1.60-mm MgF_2 compensation plate was paired with sapphire windows of varying thickness. The dotted line indicates the tolerance for retardance and depolarization of the compensated endoscope. The blue boxplots show the benchmark results from the experimental endoscope without sapphire windows.

(L–O) Mueller matrices and retardance and depolarization images measured from the PME prototype and the experimental endoscope without sapphire.

(P–R) Average retardance, depolarization, and extinction ratios of the experimental endoscope without sapphire windows, the PME, and the conventional endoscope as the FWHM of the illumination light varies. These experiments were conducted with 70° AFOV and light sources whose CWLs were 532 nm and FWHMs 10 nm and 200 nm (white-light source).



(legend on next page)

polarization-gated (PG) imaging using the PME (see Note S10), we calculated the average extinction ratio (ER) based on their Mueller matrices (Figure 2R and Note S11). The PME achieved extinction ratios comparable to those of the experimental endoscope and around 30 times higher than those of the conventional endoscope, even with white-light illumination. Overall, the PME demonstrated consistent polarization-maintaining capability with both broad- and narrowband illumination, indicating that the proposed solution can suppress the unwanted polarization effects as intended.

Imaging enhancement in the presence of specular highlights and surgical smoke

With the PME exhibiting excellent polarization-maintaining performance in the visible band, it is now possible to develop a polarization-gated white-light endoscope (PG-WLE) suitable for repeated clinical use. We demonstrate that using the PME, endoscopic color images degraded by specularities and surgical smoke can be restored with high quality. The setup of the PG-WLE system is presented in Figure 3A (for more details, see Notes S9 and S11).

To compare the PG-WLE with the computation-based approaches typically used for specular-highlight removal, the latent diffusion model (LDM)[32] was implemented as a representative method, as the LDM outperforms other popular methods and considered state of the art (see Figure S8). The PG-WLE offered the following advantages. The PG-WLE with PME can remove the specularities, whereas computation-based methods typically cannot detect all highlights and would leave areas unrestored, as indicated by blue arrows in Figures 3D–3H and 3L. To evaluate the highlight-removal performances, we calculated the percentage of highlight pixels (PHP, see Note S13). As the results show, the PHPs were reduced from 2.57%, 1.53%, and 3.79% to 1.1%, 0.21%, and 0.52%, respectively for the three scenes using the computation-based method but reduced to 0% by the PG-WLE with the PME. The PG-WLE can accurately capture the scene, while the computation-based approaches can only estimate the areas occluded by highlights from neighboring areas and often fail to reproduce the actual texture (see regions indicated by green arrows in Figures 3B–3D, 3F–3H, and 3J–3L). The PG-WLE can physically eliminate the specular reflections and capture specular-free images without computation, thereby minimizing the processing time. Consequently, the specular highlights can be removed *in vivo* in real time by the PG-WLE system with the PME (Video S1). In contrast, the LDM took approximately 2 s to restore each of the presented images (NVIDIA GeForce RTX 3090). Moreover, the cross-polarization channel of the PG-WLE removes highlights and enhances the contrast of deeper tissue targets (compare the vessels indicated by red arrows in Figures 3B–3D, 3F–3H, and 3J–3L). Furthermore, the microstructures near the tissue surface that were not visible in WLE (e.g., microcirculation indicated by the red arrow in Figure 3N) were revealed by calculating the polarization difference (PD) image with the co- and cross-polarization images (detected with polarizers aligned parallel and perpendicular to the polarization state of the incident light, respectively, see Note S12 for PD image processing).[33,34]

To validate the role of the PME in the PG-WLE system, we replaced the PME in the system with a conventional endoscope (ShenDa) and performed control experiments with it. Consider the region indicated by blue arrows in Figure 3O. Although the specular highlights are reduced in this region when the conventional endoscope is integrated into the system, a considerable amount of specularities remain due to the co- and cross-polarization channel crosstalk induced by the endoscope. The PHP of the scene decreased from 2.2% to 0.71%. Artifacts also appeared in the PD image, particularly at the corners, indicated by the green arrows in Figure 4P arising from the retardance of the endoscope. These artifacts can readily disrupt the observation of tissue. For example, the shadowy region indicated by the red arrows in Figure 3P can interfere with the interpretation of superficial microcirculation.

To evaluate the performance of smoky image restoration using the PME, we imaged the abdomen of a mouse covered by surgical smoke *in vivo* with the PG-WLE. The blood vessel, the disruptive structure on the rib cage, and the boundaries between the colon parts (indicated by red, green, and blue arrows in Figure 3Q) were unidentifiable in the smoky image (Figure 3R). Restoring the smoky images often requires estimation of parameters for the so-called image-degradation model.[35] The refined polarization difference (RPD) method developed earlier[36] was employed for parameter estimation in this study (see Note S14). The RPD method exploits both color and polarization information obtained by the PG-WLE with the PME to estimate the model parameters. Comparing Figures 3S and 3R, it is obvious that the visibility of obscured targets was substantially improved (peak signal-to-noise ratio [PSNR] of the image increased about 73%). The features indicated by the red, green, and blue arrows were restored and became identifiable (compare Figures 3S and 3Q). For comparison, we also applied the well-known dark channel prior (DCP) algorithm, a representative de-smoking technique utilizing only color information.[35]

Figure 3. Specular-highlight and surgical-smoke removal *in vivo* using the PME

(A) Using the PME to set up the PG-WLE system.

(B–M) WLE images of the oral vestibule (B), retromolar trigone (F), and buccal mucosa (J); the corresponding specular-highlights-removed images obtained using the PME (C, G, and K) and LDM algorithm (D, H, and L); and PHP of the WLE images and the specular-highlights-removed images (E, I, and M).

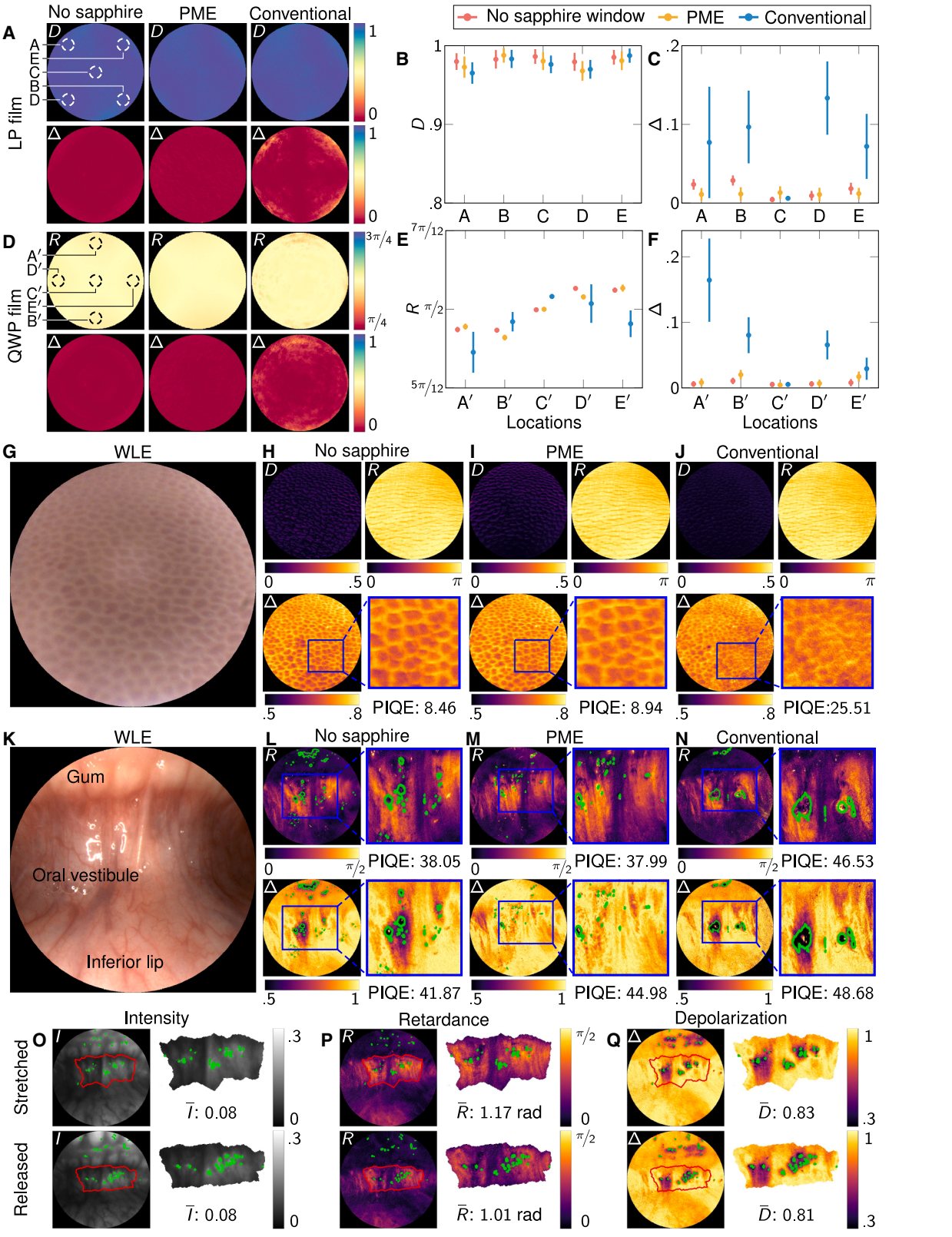
(N) The WLE image of the retromolar trigone and the corresponding PD image obtained with the PME.

(O) Specular-highlight removal results using the PG-WLE with the conventional endoscope.

(P) The WLE image and the corresponding PD image obtained using the PG-WLE system with the conventional endoscope.

(Q–U) Images of the abdomen of a mouse obtained with the PME. Ground-truth (GT) image (Q), smoky image (R), and dehazed images restored by the RPD method (S) and the DCP method (T), and the PSNR graph comparing the quality of the smoky image and the restored images (U).

(V–Z) Images of the mouse abdomen obtained with the conventional endoscope. GT image (V), smoky image (W), and dehazed image restored by the RPD (X) and DCP method (Y), and the PSNR graph comparing the quality of the smoky image and the restored image (Z).



(legend on next page)

As shown in Figure 3T, the color accuracy of the restored image was damaged, and targets such as the disruptive feature on the rib cage (indicated by the green arrow) were still difficult to identify. The images restored by the DCP are generally inferior in regard to detail recovery, with PSNRs approximately 10% lower than by RPD with the PG-WLE (Figure 3U). In comparison, the combination of color and polarimetric information obtainable by the PG-WLE with the PME results in enhanced accuracy in parameter estimation and better image restoration.

In the control experiment, the PME in the PG-WLE system was replaced by a conventional endoscope (ShenDa). The crosstalk between the co- and cross-polarization channels caused by the polarization effects of the conventional endoscope led to poor restoration performance with the RPD method. The feature on the rib cage and the boundaries between the colon sections were unidentifiable (indicated by green and blue arrows in Figure 3X). The reconstructed images lacked details and had a PSNR approximately 14% lower than the benchmark DCP result (Figures 3Y and 3Z). This is because the conventional endoscope failed to provide high-quality PG images, which are essential for the RPD method to effectively restore the image.

These experiments demonstrate that the PME is crucial for enabling PG-based endoscopic imaging techniques. It addressed challenges posed by specular reflections and surgical smoke in WLE.

Performance comparison with conventional endoscope

To demonstrate the enhancement to polarimetric endoscopy using the PME, we integrated it into the endoscopic Mueller imaging system and tested the system by performing Mueller imaging with linear polarizer (LP) and quarter waveplate (QWP) targets (see Notes S15 and S16). As shown in Figure 4A, the diattenuation and depolarization of the LP target measured by the system with the PME match the benchmark results obtained with the experimental endoscope. In contrast, the conventional endoscope introduced serious artifacts to the FOV, especially in the peripheral region. To provide quantitative analysis, we chose five representative regions of interest (ROIs A–E in Figure 4A) within the FOV and examined the mean and standard deviation of the diattenuation and depolarization in the ROIs (Figures 4B and 4C). It was demonstrated that the conventional endoscope can cause depolarization errors ten times higher than the PME in the peripheral region (ROIs A, B, D, and E). For the QWP target, we compared the retardance and depolarization (diattenuation was negligible—available in Figure S9) measured with the three endoscopes (Figure 4D) and quantitatively examined their results in ROIs A′–E′. As shown in Figure 4E, the retardance obtained by the PME and the experimental endoscope (benchmark) were almost equal (both exhibited less than 0.09 rad offset from the nominal $\pi/2$ rad in the peripheral region and around 0.01 rad standard deviations in the ROIs), whereas the results from the conventional endoscope largely deviated from the benchmark (e.g., in ROI A′ the retardance had about 0.14 rad offset from the nominal and 0.07 rad standard deviation). For the depolarization (Figure 4F), the results obtained using the PME were aligned with the benchmark, both with mean values below 0.02 and standard deviations below 0.01 in the ROIs, as expected with the QWP. In contrast, the conventional endoscope severely distorted the reconstructed depolarization image, especially in the peripheral region (e.g., in ROI A′, the depolarization mean value falsely reached 0.16 with standard deviation reaching 0.06).

Ex vivo and *in vivo* demonstrations

To validate the role of the PME in reducing noise for polarimetric endoscopy, we imaged the porcine liver tissue *ex vivo* using the endoscopic Mueller imaging system with the three endoscopes adapted sequentially. The results are presented in Figures 4G–4J and S10. It was reported that the hepatic lobules and the surrounding connective tissue exhibit polarimetric contrast.[37] The system using the PME clearly resolved this contrast, matching the benchmark (compare Figures 4H and 4I), while the system with the conventional endoscope produced noisy polarimetric images (Figure 4J). To quantitatively evaluate the quality of the reconstructed polarimetric images, we used a no-reference image-quality metric named the perception-based image-quality evaluator (PIQE; see Note S17), which assigns higher scores to noisier images. In the representative ROI (Figures 4H–4J), the PME and the experimental endoscope (benchmark) achieved similar PIQE scores of 8.46 and 8.94, respectively. In contrast, the conventional endoscope scored 25.51, indicating that its quality was three times poorer than those of the PME and the benchmark.

To validate the PME for polarimetric endoscopy, we imaged the oral vestibule *in vivo* with the three endoscopes and compared their performances. The oral vestibule was selected because it is not distinguishable from the neighboring tissues by color information with the WLE (Figure 4K) but exhibits

Figure 4. Endoscopic polarimetric imaging results

(A) Diattenuation and depolarization of the LP target measured by the experimental endoscope without sapphire windows, the PME, and the conventional endoscope, respectively.

(B and C) Mean and standard deviation of the measured diattenuation (B) and depolarization (C) in the ROIs denoted in (A).

(D) Retardance and depolarization of the QWP target measured by the experimental endoscope without sapphire windows, the PME, and the conventional endoscope, respectively.

(E and F) Mean and standard deviation of the measured retardance (E) and depolarization (F) in the ROIs denoted in (D).

(G) WLE image of the *ex vivo* porcine liver tissue.

(H–J) Diattenuation, retardance, and depolarization and the representative ROI images obtained by the endoscopic Mueller imaging system with the experimental endoscope without sapphire windows (H), the PME (I), and the conventional endoscope (J) incorporated into the system.

(K) WLE image of the human oral vestibule.

(L–N) Retardance and depolarization images obtained by snapshot endoscopic Stokes imaging system with the experimental endoscope without sapphire windows (L), the PME (M), and the conventional endoscope (N) incorporated into the system, and the corresponding ROI images.

(O–Q) Intensity (O), retardance (P), and depolarization (Q) images and the ROIs (bordered by the red lines) of the oral vestibule when it was stretched and relaxed. In (L)–(Q), the areas circled by the green lines are invalid due to saturation by specular highlights.

considerable retardance owing to the rich connective tissues.[21] Since the *in vivo* target was constantly moving, a snapshot endoscopic Stokes imaging system was constructed for the experiment (see Notes S18 and S19). As the results show (Figures 4K–4N and S12), the PME provided polarimetric images (PIQE scored 37.99 and 44.98, respectively for retardance and depolarization images, Figure 4L) with qualities close to the benchmark experimental endoscope (PIQE scored 38.05 and 41.87, respectively for retardance and depolarization images, Figure 4M). In contrast, the quality of the retardance and depolarization images obtained with the conventional endoscope was 22% and 7% poorer, respectively (PIQE scored 46.53 and 48.68, Figure 4N). In Figures 4L–4N, the images were captured at different times. The discrepancy observed in the depolarization images between Figures 4L and 4M arise from changes in specular reflection regions, resulting from movement of the tissue and the endoscope. Note that the image-quality evaluation was not affected. Additionally, we utilized the PME to characterize the polarization properties of the oral vestibule *in vivo* when it is stretched and released. Our results indicate that the intensity remained essentially unaffected by the applied tension, as evidenced by the consistent intensities in the tracked region (Figure 4O). Meanwhile, the depolarization slightly increased with the applied tension, arising likely because of stronger tissue birefringence induced by the tension (Figure 4Q). Retardance exhibited a remarkable rise (Figure 4P), suggesting better alignment of the connective tissue induced by the increasing tension. These results were consistent with those reported by previous research.[37]

These experiments demonstrate that the PME is crucial for reducing errors and improving the quality of polarimetric endoscopy. The technique enables consistent and reliable characterization of tissue from a perspective beyond color, potentially enhancing lesion-detection precision.

Conclusion and outlook

An endoscope with sapphire windows that maintains polarization in the visible spectrum has been investigated for potential clinical translation of polarization-resolved imaging techniques. Here, we present a viable solution to the conflict between ''maintaining polarization'' and ''sapphire windows.'' The constructed PME prototype addresses challenges in the color-resolved WLE including image degradation caused by specularities and surgical smoke as well as improving the quality of polarimetric imaging.

Compared to previous studies,[24] a deeper insight into the polarization effects of conventional endoscopes is provided in this work, encompassing all factors influencing these effects and their formation mechanisms. Based on the study, it is found that depolarization in conventional endoscopes is essentially the secondary effects of retardance inhomogeneity and can thus be suppressed by manipulating the retardance via birefringence compensation. Additionally, the influence of the endoscope aperture (i.e., entrance pupil) on depolarization is not negligible, given its small diameter (sub-millimeter magnitude). This finding explained the remaining depolarization observed with quasi-monochromatic illumination, which was shown but not noted or explained in previous literature.[23]

The proposed approach based on birefringence compensation to achieve the broadband PME requires minimal modification to the standard optical design and fabrication process of the conventional endoscope. Therefore, the optical design of the endoscope and the key fabrication procedures are minimally affected. The tolerance for thickness mismatch is in the range of tens of micrometers, and tolerance for OA misalignment is in several degrees. These tolerances are several orders of magnitude higher than the typical machining and alignment precision in optics. As a result, the approach imposes minimal additional burden on the process of endoscope fabrication.

The polarization-maintaining performance of the PME in the visible band enables seamless fusion of the polarization- and color-resolved imaging modalities. This approach not only avoids the limitations of color-only imaging, such as visual obstruction and confusing features caused by specularities, but also obtains the standard color-resolved image equivalent to WLE. The polarimetric endoscopy experiments here demonstrated that polarimetric properties of tissue related to tissue histopathological features[38–40] can be obtained with better accuracy using the PME. Nevertheless, based on this study, for applications that tolerate more errors and noise, it is feasible to conduct polarimetric endoscopy with conventional endoscopes whose polarization effects are mitigated by, for example, reducing sapphire thickness or AFOV followed by numerical calibration.

As a key component for polarization-resolved endoscopy, the PME keeps the sapphire windows, which makes it safe and durable for use and removes a major barrier for the clinical translation of polarization-resolved endoscopy. We also show that polarization-resolved endoscopy based on the PME can effectively address the challenges of standard color-resolved WLE and pave the way for precision and intelligent MIS.

We also note some limitations of this work. The proposed solution for achieving a PME will lead to higher costs, primarily due to the inclusion of an additional compensation plate and the extra alignment efforts during assembly. The PME was modified to have negligible polarization effects under broadband illumination. It was not experimentally validated whether it maintains polarization under every wavelength in the visible spectrum. However, by inference, the PME should well maintain the polarization states for every wavelength within the visible spectrum.

METHODS

Details regarding the methods can be found in the supplemental information.

RESOURCE AVAILABILITY

Lead contact

Requests for further information and resources should be directed to and will be fulfilled by the lead contact, Ji Qi (ji.qi@zhejianglab.org).

Materials availability

The materials generated in this study are available from the lead contact upon reasonable request.

Data and code availability

The data and code supporting the results in this study are available within the paper and its supplemental information. Requests for further information should be directed to the lead contact.

ACKNOWLEDGMENTS

This research was supported by the National Natural Science Foundation of China (grant nos. T2293752, T2293750, and 61905152), the Zhejiang Provincial Natural Science Foundation of China (grant no. LR23F050001), the Key R&D Program of Zhejiang (grant no. 2024SSYS0014), and fellowship of the China Postdoctoral Science Foundation (grant no. 2022M722908).

AUTHOR CONTRIBUTIONS

J.Q. and J.S. conceptualized the study. J.S. performed the experiments and carried out device engineering. C.Z. performed the computation-based specular-highlight removal. D.W. performed image restoration for images affected by surgical smoke. L.W. and F.G. fabricated the experimental endoscopes. J. S., J.Q., and Y.C. wrote the manuscript. J.Q., J.S., X.Y., Q.Y., and D.S.E. reviewed and commented on the manuscript.

DECLARATION OF INTERESTS

The Zhejiang Lab has filed a patent application describing the method for constructing the PME (application no. CN202310129365.3; authors J.Q. and J.S.).

SUPPLEMENTAL INFORMATION

Supplemental information can be found online at https://doi.org/10.1016/j.device.2025.100871.

Received: January 6, 2025
Revised: March 28, 2025
Accepted: July 4, 2025
Published: August 4, 2025

REFERENCES

1. Ali, S., Zhou, F., Bailey, A., Braden, B., East, J.E., Lu, X., and Rittscher, J. (2021). A deep learning framework for quality assessment and restoration in video endoscopy. Med. Image Anal. *68*, 101900. https://doi.org/10.1016/j.media.2020.101900.
2. Kudva, V., Prasad, K., and Guruvare, S. (2017). Detection of Specular Reflection and Segmentation of Cervix Region in Uterine Cervix Images for Cervical Cancer Screening. Irbm *38*, 281–291. https://doi.org/10.1016/j.irbm.2017.08.003.
3. Ulmer, B.C. (2008). The Hazards of Surgical Smoke. AORN J. *87*, 721–738. https://doi.org/10.1016/j.aorn.2007.10.012.
4. Daher, R., Vasconcelos, F., and Stoyanov, D. (2023). A Temporal Learning Approach to Inpainting Endoscopic Specularities and Its Effect on Image Correspondence. Med. Image Anal. *90*, 102994. https://doi.org/10.1016/j.media.2023.102994.
5. Li, R., Pan, J., Si, Y., Yan, B., Hu, Y., and Qin, H. (2020). Specular Reflections Removal for Endoscopic Image Sequences With Adaptive-RPCA Decomposition. IEEE Trans. Med. Imaging *39*, 328–340. https://doi.org/10.1109/TMI.2019.2926501.
6. Stoyanov, D., and Yang, G.Z. (2005). Removing specular reflection components for robotic assisted laparoscopic surgery. IEEE Int. Conf. Image Process. *3*, III-632. https://doi.org/10.1109/ICIP.2005.1530471.
7. Lier, M.C.I., Vlek, S.L., Ankersmit, M., van de Ven, P.M., Dekker, J.J.M.L., Bleeker, M.C.G., Mijatovic, V., and Tuynman, J.B. (2020). Comparison of enhanced laparoscopic imaging techniques in endometriosis surgery: a diagnostic accuracy study. Surg. Endosc. *34*, 96–104. https://doi.org/10.1007/s00464-019-06736-8.
8. Menon, S., Dhar, A., Hoare, J.M., and Trudgill, N. (2012). How commonly is gastric cancer missed at endoscopy: a UK primary care based study. Gastrointest. Endosc. *75*, AB139. https://doi.org/10.1016/j.gie.2012.04.060.
9. He, K., Sun, J., and Tang, X. (2011). Single Image Haze Removal Using Dark Channel Prior. IEEE Trans. Pattern Anal. Mach. Intell. *33*, 2341–2353. https://doi.org/10.1109/TPAMI.2010.168.
10. Pahlevaninezhad, H., Khorasaninejad, M., Huang, Y.-W., Shi, Z., Hariri, L. P., Adams, D.C., Ding, V., Zhu, A., Qiu, C.W., Capasso, F., and Suter, M.J. (2018). Nano-optic endoscope for high-resolution optical coherence tomography *in vivo*. Nat. Photonics *12*, 540–547. https://doi.org/10.1038/s41566-018-0224-2.
11. DePaoli, D., Côté, D.C., Bouma, B.E., and Villiger, M. (2022). Endoscopic imaging of white matter fiber tracts using polarization-sensitive optical coherence tomography. Neuroimage *264*, 119755. https://doi.org/10.1016/j.neuroimage.2022.119755.
12. Zhang, L., Pleskow, D.K., Turzhitsky, V., Yee, E.U., Berzin, T.M., Sawhney, M., Shinagare, S., Vitkin, E., Zakharov, Y., Khan, U., et al. (2017). Light scattering spectroscopy identifies the malignant potential of pancreatic cysts during endoscopy0040. Nat. Biomed. Eng. *1*. https://doi.org/10.1038/s41551-017-0040.
13. Pleskow, D.K., Sawhney, M.S., Upputuri, P.K., Berzin, T.M., Coughlan, M. F., Khan, U., Glyavina, M., Zhang, X., Chen, L., Sheil, C.J., et al. (2023). In vivo detection of bile duct pre-cancer with endoscopic light scattering spectroscopy. Nat. Commun. *14*, 109. https://doi.org/10.1038/s41467-022-35780-7.
14. Waldner, M.J., Wirtz, S., Neufert, C., Becker, C., and Neurath, M.F. (2011). Confocal laser endomicroscopy and narrow-band imaging-aided endoscopy for in vivo imaging of colitis and colon cancer in mice. Nat. Protoc. *6*, 1471–1481. https://doi.org/10.1038/nprot.2011.377.
15. Liang, W., Hall, G., Messerschmidt, B., Li, M.-J., and Li, X. (2017). Nonlinear optical endomicroscopy for label-free functional histology in vivo. Light Sci. Appl. *6*, e17082. https://doi.org/10.1038/lsa.2017.82.
16. Waterhouse, D.J., Fitzpatrick, C.R.M., Pogue, B.W., O'Connor, J.P., and Bohndiek, S.E. (2019). A roadmap for the clinical implementation of optical-imaging biomarkers. Nat. Biomed. Eng. *3*, 339–353. https://doi.org/10.1038/s41551-019-0392-5.
17. Morgan, S.P., and Stockford, I.M. (2003). Surface-reflection elimination in polarization imaging of superficial tissue. Opt. Lett. *28*, 114–116. https://doi.org/10.1364/OL.28.000114.
18. Hu, H., Han, Y., Li, X., Jiang, L., Che, L., Liu, T., and Zhai, J. (2022). Physics-informed neural network for polarimetric underwater imaging. Opt. Express *30*, 22512–22522. https://doi.org/10.1364/oe.461074.
19. Zhou, C., Teng, M., Han, Y., Xu, C., and Shi, B. (2024). Learning to Dehaze with polarization. Adv. Neural Inf. Process. Syst. *34*, 11487–11500. https://doi.org/10.5555/3540261.3541139.
20. He, C., He, H., Chang, J., Chen, B., Ma, H., and Booth, M.J. (2021). Polarisation optics for biomedical and clinical applications: a review. Light Sci. Appl. *10*, 194. https://doi.org/10.1038/s41377-021-00639-x.
21. Qi, J., Tatla, T., Nissanka-Jayasuriya, E., Yuan, A.Y., Stoyanov, D., and Elson, D.S. (2023). Surgical polarimetric endoscopy for the detection of laryngeal cancer. Nat. Biomed. Eng. *7*, 971–985. https://doi.org/10.1038/s41551-023-01018-0.
22. Tumanova, K., Serra, S., Majumdar, A., Lad, J., Quereshy, F., Khorasani, M., and Vitkin, A. (2023). Mueller matrix polarization parameters correlate with local recurrence in patients with stage III colorectal cancer. Sci. Rep. *13*, 13424. https://doi.org/10.1038/s41598-023-40480-3.
23. He, L., Chen, C., Li, H., Li, Y., and Yi, R. (2022). Research advances in joining processes of sapphire. Int. J. Adv. Manuf. Technol. *121*, 59–81. https://doi.org/10.1007/s00170-022-09199-9.
24. Wood, T.C., and Elson, D.S. (2010). Polarization response measurement and simulation of rigid endoscopes. Biomed. Opt. Express *1*, 463–470. https://doi.org/10.1364/boe.1.000463.

25. Lindberg, A., Gennet, C., Vizet, J., Vanel, J.-C., and Pierangelo, A. (2019). Mueller polarimetric imaging through a rigid endoscope. European Conference on Biomedical Optics (Optica Publishing Group), p. 11073. https://doi.org/10.1117/12.2526384.

26. Qi, J., Barrière, C., Wood, T.C., and Elson, D.S. (2012). Polarized multispectral imaging in a rigid endoscope based on elastic light scattering spectroscopy. Biomed. Opt. Express *3*, 2087–2099. https://doi.org/10.1364/boe.3.002087.

27. Trout, R.M., Gnanatheepam, E., Gado, A., Reik, C., Ramella-Roman, J.C., Hunter, M., Schnelldorfer, T., and Georgakoudi, I. (2022). Polarization enhanced laparoscope for improved visualization of tissue structural changes associated with peritoneal cancer metastasis. Biomed. Opt. Express *13*, 571–589. https://doi.org/10.1364/boe.443926.

28. Qi, J., Ye, M., Singh, M., Clancy, N.T., and Elson, D.S. (2013). Narrow band 3x3 Mueller polarimetric endoscopy. Biomed. Opt. Express *4*, 2433–2449. https://doi.org/10.1364/BOE.4.002433.

29. Qi, J., and Elson, D.S. (2016). A high definition Mueller polarimetric endoscope for tissue characterisation. Sci. Rep. *6*, 25953. https://doi.org/10.1038/srep25953.

30. Garcia, M., and Gruev, V. (2017). Optical characterization of rigid endoscopes and polarization calibration methods. Opt. Express *25*, 15713–15728. https://doi.org/10.1364/oe.25.015713.

31. He, C., Chang, J., Hu, Q., Wang, J., Antonello, J., He, H., Liu, S., Lin, J., Dai, B., Elson, D.S., et al. (2019). Complex vectorial optics through gradient index lens cascades. Nat. Commun. *10*, 4264. https://doi.org/10.1038/s41467-019-12286-3.

32. Rombach, R., Blattmann, A., Lorenz, D., Esser, P., and Ommer, B. (2022). High-resolution image synthesis with latent diffusion models. In Proceedings of IEEE/CVF Conference on Computer Vision and Pattern Recognition (CVPR), pp. 10684–10695. https://doi.org/10.1109/cvpr52688.2022.01042.

33. Jacques, S.L., Ramella-Roman, J.C., and Lee, K. (2002). Imaging skin pathology with polarized light. J. Biomed. Opt. *7*, 329–340. https://doi.org/10.1117/1.1484498.

34. Clancy, N.T., Arya, S., Qi, J., Stoyanov, D., Hanna, G.B., and Elson, D.S. (2014). Polarised stereo endoscope and narrowband detection for minimal access surgery. Biomed. Opt. Express *5*, 4108–4117. https://doi.org/10.1364/boe.5.004108.

35. Lee, S., Yun, S., Nam, J.-H., Won, C.S., and Jung, S.-W. (2016). A review on dark channel prior based image dehazing algorithms. EURASIP J. Image Video Process. *2016*, 4–23. https://doi.org/10.1186/s13640-016-0104-y.

36. Wang, D., Song, J., Gao, J., Qi, J., and Elson, D.S. (2024). Computational polarization imaging in vivo through surgical smoke using refined polarization difference. Adv. Sci. *11*, e2309998. https://doi.org/10.1002/advs.202309998.

37. Qi, J., He, H., Lin, J., Dong, Y., Chen, D., Ma, H., and Elson, D.S. (2018). Assessment of tissue polarimetric properties using Stokes polarimetric imaging with circularly polarized illumination. J. Biophotonics *11*, e201700139. https://doi.org/10.1002/jbio.201700139.

38. Pierangelo, A., Manhas, S., Benali, A., Fallet, C., Totobenazara, J.L., Antonelli, M.R., Novikova, T., Gayet, B., De Martino, A., and Validire, P. (2013). Multispectral Mueller polarimetric imaging detecting residual cancer and cancer regression after neoadjuvant treatment for colorectal carcinomas. J. Biomed. Opt. *18*, 046014. https://doi.org/10.1117/1.jbo.18.4.046014.

39. Qi, J., and Elson, D.S. (2017). Mueller polarimetric imaging for surgical and diagnostic applications: a review. J. Biophotonics *10*, 950–982. https://doi.org/10.1002/jbio.201600152.

40. Li, P., Dong, Y., Wan, J., He, H., Aziz, T., and Ma, H. (2021). Polaromics: deriving polarization parameters from a Mueller matrix for quantitative characterization of biomedical specimen. J. Phys. D Appl. Phys. *55*, 034002. https://doi.org/10.1088/1361-6463/ac292f.